



**HAL**  
open science

## **Transitional shockwave/boundary layer interaction experiments in the R2Ch blowdown wind tunnel**

Mathieu Lugin, François Nicolas, Nicolas Severac, Jean-Pierre Tobeli, Samir Beneddine, Eric Garnier, Sebastien Esquieu, Reynald Bur

► **To cite this version:**

Mathieu Lugin, François Nicolas, Nicolas Severac, Jean-Pierre Tobeli, Samir Beneddine, et al.. Transitional shockwave/boundary layer interaction experiments in the R2Ch blowdown wind tunnel. Experiments in Fluids, 2022, 63 (2), pp.46. 10.1007/s00348-022-03395-9 . hal-03584421

**HAL Id: hal-03584421**

**<https://hal.science/hal-03584421>**

Submitted on 22 Feb 2022

**HAL** is a multi-disciplinary open access archive for the deposit and dissemination of scientific research documents, whether they are published or not. The documents may come from teaching and research institutions in France or abroad, or from public or private research centers.

L'archive ouverte pluridisciplinaire **HAL**, est destinée au dépôt et à la diffusion de documents scientifiques de niveau recherche, publiés ou non, émanant des établissements d'enseignement et de recherche français ou étrangers, des laboratoires publics ou privés.

# Transitional shockwave/boundary layer interaction experiments in the R2Ch blowdown wind tunnel

Mathieu Lugrin · François Nicolas · Nicolas Severac · Jean-Pierre Tobeli · Samir Beneddine · Eric Garnier · Sebastien Esquieu · Reynald Bur

Received: date / Accepted: date

**Abstract** Transitional Shockwave/Boundary Layer Interactions (SBLI) is studied experimentally. Experiments are conducted on a hollow-cylinder flare model in the R2Ch blowdown facility at a Mach number of 5 for three different Reynolds numbers in the transitional regime. Unsteady wall pressure measurements are conducted along with mean and unsteady heat flux measurements and high-speed Schlieren imaging. The images are then processed using Proper Orthogonal Decomposition (POD) and Spectral Proper Orthogonal Decomposition (SPOD) to extract relevant information. Two main phenomena are identified and documented: the oblique modes traveling in the shear layer above the recirculation region and the streaks appearing in the reattachment region. New results illustrating the multiple physical origins of the streaks, either linked with globally unstable modes and convectively unstable mechanisms, are discussed.

**Keywords** Hypersonic · Shock-wave · Boundary layer · Transition

## 1 Introduction

The proper understanding and prediction of laminar-turbulent transition is one of the current limiting factor for the development of hypersonic flight. For example, for generic (*e.g.* attached boundary layer) cases, the heat flux overshoots drastically in the transition region,

---

M. Lugrin · F. Nicolas · N. Severac · J.P. Tobeli · S. Beneddine · E. Garnier · R. Bur  
DAAA, ONERA, Paris Saclay University, F-92190 Meudon - France  
E-mail: mathieu.lugrin@onera.fr

S. Esquieu  
CESTA, CEA, F-33114 Le Barp - France

with a transition onset highly dependent on the flight conditions, making the correct design of the thermal protection tedious. Adding to that complexity, shocks appear in the vicinity of any geometrical discontinuities presents on vehicles, such as control surface or inlets compression ramps. Those shocks interact with the boundary layer and may cause the apparition of a recirculation downstream from the interaction.

First, key parameters such as the Reynolds number (Benay et al., 2006; Heffner et al., 1993) or free-stream perturbation levels (Lugrin et al., 2021b) are known to significantly impact the topology of transitional flows. An increase of any of these parameters leads to a change in recirculating region size and heat-flux distribution. Understanding the flow behavior in this region is crucial as the recirculation region appears at the foot of critical flight apparatus. Small changes in flow topology (*i.e.* the position of the separation and reattachment points and the recirculation region size) may lead to drastic changes of the control surface responsiveness, or of the propulsion system efficiency. In addition, the heat-flux levels at reattachment may be more than ten times higher than in the separated region (see for instance Benay et al. (2006); Bur and Chanetz (2009)). Thus, any uncertainty on the reattachment location leads to strongly over(or under)-predicted thermal loads. Previous results from Bur and Chanetz (2009) showed how crucial is the prediction of the correct transitional heat-flux in the reattachment region for real life designs such as the Pre-X vehicle.

Even if it is critical for vehicle design, the literature on the transition to turbulence through hypersonic Shockwave/Boundary Layer Interactions (SBLI) remains limited. Multiple experimental and numerical studies on hypersonic attached boundary layer point toward second mode waves being the dominant linear

instability and thus being responsible for transition. High-frequency pressure signal corresponding to such instabilities have been recorded in numerous experiments (Estorf et al., 2008; Chynoweth et al., 2019). Such experiments, coupled with local linear stability analyses (Mack, 1975; Özgen and Kirca, 2008; Esquieu et al., 2019), unveil the importance of second mode for hypersonic transition. However, Franko and Lele (2013, 2014) have shown that oblique first mode instabilities may also play an important role in the transition process. The separated region may also bring new transitional mechanisms; for instance, recent experiments from Benitez et al. (2020) have shown that the shear layer generates new instabilities. Those three-dimensional shear-layer oblique supersonic type instabilities may become the dominant linear instability above the separated region (Sandham and Reynolds, 1990; Reynolds, 1991; Kudryavtsev and Khotyanovsky, 2005; Foyi and Sarkar, 2010).

Since the early work of Ginoux (1969), the presence of streaks in the reattachment region of SBLI has been reported. For instance, Benay et al. (2006); Murray et al. (2013) used oil-flow visualization to document the presence of steady streaks (one has to keep in mind that the oil flow may be stabilizing the streaks, forcing them to be steady (Murray et al., 2013)) on the configuration studied here. Görtler-like vortices appears to be Reynolds independent (Aymer De La Chevalerie et al., 1997) and related to the experiment and model geometry. Indeed, Chuvakhov et al. (2017) showed that blunt leading edge and increase in the ramp angle leads to a decrease in the vortex intensity. The extensive work of Vermeulen and Simeonides (1992); Simeonides (1992); Simeonides and Haase (1995) confirmed the footprints of Görtler-like vortices developing on concave walls thanks to infrared visualizations. Roghelia et al. (2017); Aymer De La Chevalerie et al. (1997) further visualized the streaks with infrared measurements in SBLI cases. More recently, Pressure and Temperature Sensitive Paints (PSP and TSP) have also been used (Chuvakhov et al., 2017; Yang et al., 2012; Gonzales et al., 2020) to capture the streaks pattern in the reattachment region. Running and Juliano (2021) also reported weak wall pressure and temperature signature of quasi-steady streaks in their unsteady PSP measurements. In a preliminary study Running et al. (2020) also reported information about the Stanton number signature of the streaks using IR imaging, alongside a first attempt to quantify the streaks' wavelength using spectral analysis.

The origin of streaks in SBLI is still under heavy debate; multiple mechanisms that could lead to their presence are documented in the numerical literature. Comte (1999) was the first to document the presence

of streamwise vortices in a LES of a turbulent compression ramp interaction that he assumed were Görtler vortices. His work was followed by the DNS of a similar configuration by Adams (2000) which came to the same conclusion. Latter, Navarro-Martinez and Tutty (2005) presented similar results for laminar interactions.

However, the mechanism proposed by Görtler (1940) is not the only one that can lead to steady vortices. For instance, the numerical work of Sandham and Reynolds (1990) showed that the oblique waves present in the mixing layer could create elongated streamwise structures through strong baroclinic and dilatational effects. Recently, Dwivedi et al. (2019) conducted an input-output analysis on a compression ramp base flow to demonstrate that the streaks could be directly caused by a convective baroclinic mechanism. Lugin et al. (2021b) showed that the receptivity process of convective mechanisms could also be altered by non-linear interaction of boundary layer modes, similarly to what happens in boundary layers for oblique breakdown. Sidharth et al. (2018); Hildebrand et al. (2018) showed that a global instability growing inside the bubble could also cause striation in the reattachment region for laminar and transitional SBLI. Finally, Cao et al. (2021) unveiled that the non-linear saturation of those global modes could also lead to striation in fully laminar cases.

The present work aims at experimentally simulating a canonical transitional SBLI configuration to document the transitional instabilities and the change in flow topology. It is a continuation of previous studies from Benay et al. (2006); Bur and Chanetz (2009) which focuses on the same geometry and overall similar flow conditions. A photograph of the cylinder-flare model in the R2Ch facility is presented in figure 1. The flow conditions for the runs are summarized in table 1, they range from low transitional flow at  $Re_L = 4 \times 10^5$  to high transitional flow for  $Re_L = 1.1 \times 10^6$ . Following the work of Benay et al. (2006); Threadgill et al. (2021); Lugin et al. (2021b,a) on transitional shockwave/boundary layer interaction, the conditions chosen for this study yield a fully laminar flow up to the separation point followed by a transitional reattachment. The interaction of shockwave with a transitional boundary layer is not documented in this article. The laminar/transitional/turbulent nature of each region of the flow is further discussed in a dedicated section (§3.1).

Compared to the previous studies of Benay et al. (2006); Bur and Chanetz (2009), new means of investigation, in particular high-speed acquisitions, allowed us to explore the complex flow dynamics. Unsteady pressure measurements have been conducted alongside high-speed Schlieren and infrared thermography. The goals of the present study are threefold: first, the impact

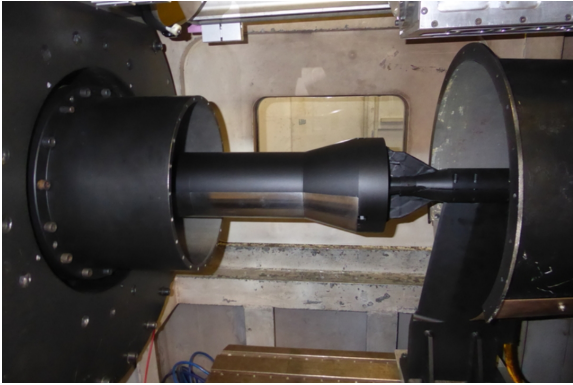


**Fig. 1** Model in the R2Ch blowdown facility

$M_\infty$	5	5	5
$Re_L$	$4 \times 10^5$	$7 \times 10^5$	$1.1 \times 10^6$
<b>Run 1</b>			
$T_{st}(K)$	$504 \pm 0.6$	$524 \pm 0.6$	$547 \pm 0.9$
$P_{st}(Pa)$	$1.27 \times 10^5 \pm 480$	$2.41 \times 10^5 \pm 762$	$4.14 \times 10^5 \pm 1157$
<b>Run 2</b>			
$T_{st}(K)$	$503 \pm 0.6$	$525 \pm 0.7$	$553 \pm 0.8$
$P_{st}(Pa)$	$1.29 \times 10^5 \pm 459$	$2.25 \times 10^5 \pm 657$	$4.08 \times 10^5 \pm 1266$

**Table 1** Mean free-stream conditions and standard deviation computed on a 2-second window during the high-frequency acquisition. The Reynolds number are computed from run 1.

of the Reynolds number on the flow topology will be documented and compared to the literature; secondly, the streaky pattern on the flare will be investigated using imaging coupled with post-processing tools such as Proper Orthogonal Decomposition (POD). Finally, unsteady pressure transducers and Schlieren imaging will be used to document the mixing layer modes present on top of the recirculation region.

## 2 Experimental setup

### 2.1 Facility

The R2Ch facility in the ONERA Meudon site was used for the experiments. The facility is a conventional blowdown wind tunnel (test duration between 15 and 30 seconds) equipped with a set of contoured axisymmetric nozzles covering a Mach number range from 5 to 7 (here, a 0.327m exit diameter Mach 5 nozzle is used). A schematic of the facility is presented in figure 2. The R2Ch wind tunnel is a cold hypersonic facility: the stagnation temperature is raised to a level just sufficient to prevent air liquefaction during expansion in the nozzle. Upstream air is heated to a stagnation temperature  $T_{st}$  slightly above 500K ( $510K < T_{st} < 550K$ ) by streaming through a Joule-effect heater. The stagnation pressure may be controlled to range from lami-

nar/low transitional to fully turbulent Reynolds number. In the present experiments, stagnation pressures  $P_{st}$  are chosen in the range  $1.3 \times 10^5 \text{ Pa} < P_{st} < 4.1 \times 10^5 \text{ Pa}$ . This leads to Reynolds numbers which range from  $Re_L = 4 \times 10^5$  to  $Re_L = 1.14 \times 10^6$ . The free-stream static pressure fluctuations of the wind tunnel have been measured to be  $1.7\% \pm 0.1\%$ , for all the operating conditions presented in this paper, using a 150mm long  $5^\circ$  half angle sharp cone equipped with a kulite (90mm downstream of the tip of the cone) and a PCB sensor (105mm downstream of the tip of the cone). According to a previous study conducted by Masutti et al. (2011), this method should yield results similar to the more traditional pitot probe measurements.

The leading edge of the model is positioned 140 mm upstream from the nozzle exit, at  $0^\circ$  angle of attack and  $0^\circ$  yaw angle. This ensures that the model is entirely located inside the Mach 5 rhombus and that there is no blockage effect. The angle of attack is first set by using an inclinometer. It is then validated using the symmetry of the shock system on the lower and upper part of the model using a dedicated Schlieren setup. The final angle of attack in wind referential is  $\alpha = 0^\circ \pm 0.05^\circ$  (the final uncertainty is set by the ability to measure the angles from the Schlieren images). The yaw angle is measured in the nozzle referential using a depth gauge to be  $\beta = 0.004^\circ \pm 0.0002^\circ$ . However, it may slightly depart from  $0^\circ$  in the true wind referential, which can explain the weak curvature of the reattachment line visible in figure 6. While this misalignment may have an effect on the development of the instabilities studied in this article, recent results from Benitez et al. (2021) show that this impact is rather limited in conventional wind tunnel due to the presence of free-stream noise, as they reported similar streaks for angle varying from 0 to  $0.3^\circ$ .

The time evolutions of the stagnation pressure and temperature during a typical run (in this case  $Re_L = 1.14 \times 10^6$ ) are presented in figure 3 alongside the time were the different measurements are conducted. The high-speed unsteady data are acquired near the end of the run, when the flow is fully established and the Reynolds number almost constant. Due to constraints intrinsic to the facility, one can never achieve a fully constant stagnation temperature (as the whole system is slowly heating during the run). Yet, the Reynolds number change during the run is negligible, and the flow conditions can be considered constant over time during the high-speed acquisition. Thus, the operating conditions that are presented in table 1 are computed as an average over a 2-second window during the high-speed acquisition. Two runs are presented since two different acquisitions are needed for the infrared imaging (one at



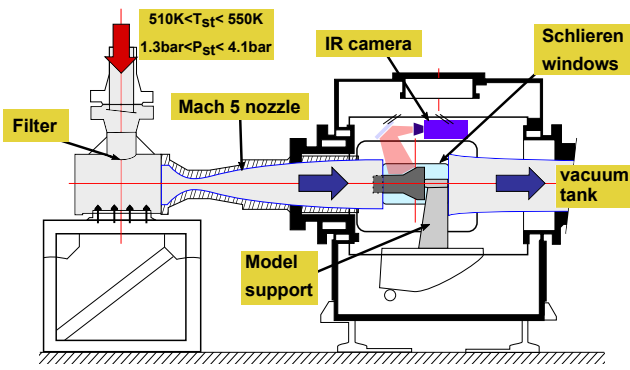


Fig. 2 Schematic of the R2Ch facility

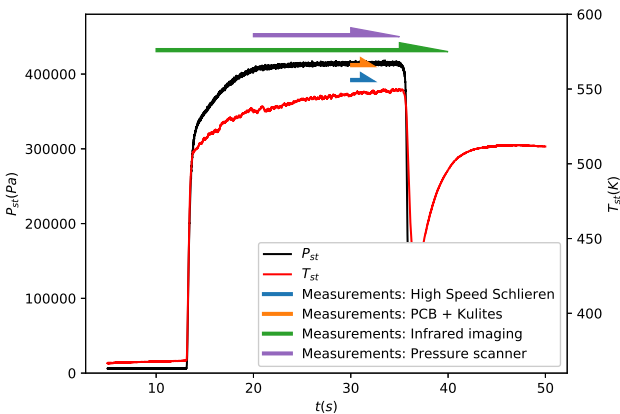


Fig. 3 Time evolution of stagnation conditions during a run and time acquisitions of several measurements during the run.

full frame, and one at reduced frame, see section 2.3). The Reynolds numbers are computed from the first run. One may see that there is an excellent reproducibility of the runs for  $Re_L = 4 \times 10^5$  and  $Re_L = 1.1 \times 10^6$  (at most 1.5% difference between each run), but a less good one for  $Re_L = 7 \times 10^5$  (7% change in  $P_{st}$  between run 1 and 2). The difference between the two runs at  $Re_L = 7 \times 10^5$  can be attributed to the difficulty to precisely regulate the pressure level upstream of the blow-down wind tunnel. The reproducibility of the unsteady measurements between similar runs is verified by comparing kulite pressure spectrums (not shown) and is found to be very good, even for the case  $Re_L = 7 \times 10^5$ .

## 2.2 Model and instrumentation

The model used for the experiments is a refurbished version of the model from the experiments of Vandomme (2004). It is a hollow cylinder of outer diameter  $D_{out} = 131\text{mm}$ , inner diameter  $D_{in} = 108\text{mm}$  and length  $L = 252\text{mm}$  with a sharp leading edge (measured radius of  $27.5 \pm 1\mu\text{m}$ ), followed by a  $15^\circ$  flare. The total length of interest is  $350\text{mm}$ . The flare itself is then followed by a

50-mm-long cylindrical extension to minimize the base flow influence on the interaction region, giving a total model length of  $400\text{mm}$ . This model was designed to be able to have a separated flow in transitional conditions. The hollow geometry is a key design feature of this experiment, as it allows a large model to be used in the facility without obstructing the test section by a blockage effect, which would impact the starting phase of the facility. While both the inside and outside structures of the model are reused, the model has been reequipped and resurfaced. The model is made of Isotan, with a Nimonic leading edge, and is half painted in black for infrared imaging. The rugosity of the painted part of the model has been measured using a Marh MarSurf M 400 and is  $Ra < 3.2\mu\text{m}$ , while the rugosity of the bare-metal part of the model is  $Ra < 1.2\mu\text{m}$ . The temperature of the model was measured to vary only slightly during the runs ( $< 15\text{K}$  on the flare,  $< 2\text{K}$  on the cylinder) and a good approximation for numerical reproduction of the present experiments could be to use an isothermal wall at  $\sim 290\text{K}$ . A view of the model, including the sensors, can be seen in figure 4.

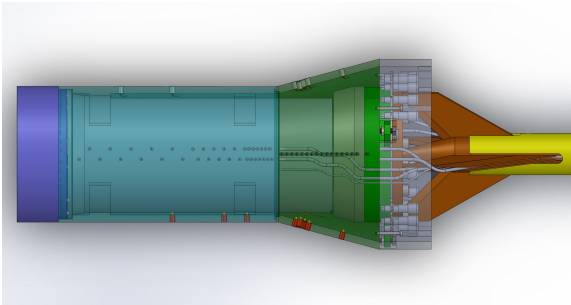
The 52 pressure taps distributed along the model as in previous experiments (Vandomme, 2004; Benay et al., 2006) are kept and provide measurements of the mean pressure distribution along the geometry. Those pressure taps are connected to electronic pressure scanners (ESP32) via stainless-steel tubes prolonged by flexible silicon tubes. Pressure ports are addressed using the digital I/O bank of a NI PXIe 6361 which performs digitization of each sensor signal. The uncertainty on the pressure scanner measurements is estimated to be  $\pm 10\%$ . The signals of wind tunnel parameters ( $P_{st}$ ,  $T_{st}$ , etc.) are acquired using a NI PXI 6284 multiplexer. The main modification on the model is the presence of 7 Kulite XCQ-093 (1Psi differential range and B type screened) and 4 PCB 132A31 sensors for unsteady pressure fluctuation measurements. Positions of those sensors can be found in tables 2 and 3. The PCB sensors are conditioned by a 4-channel PCB 482C05 signal conditioner free of any amplification and filtering, the output is then digitized by a NI PXIe-6376 with a sampling frequency set to  $3.3\text{MHz}$ . While the acquisition permits very high-frequency measurements with PCB sensors, one has to be careful when interpreting results at frequencies higher than  $300\text{kHz}$  as resonance was observed during shock-tube calibration of those sensors (see appendix 1); this resonance is also mentioned in other studies (Butler and Laurence, 2021a; Grossir, 2017). A special model integration technique has been used for PCB sensors and is described in appendix 1. This technique yields both a better flush mount and a thermal protection of the sensor. For the Kulites sen-

**Table 2** PCB132A31 sensors position. Measurement origin is the leading edge of the model.

PCB	1	2	3	4
$\frac{X}{L}$	1.07	1.09	1.10	1.12

**Table 3** Kulite sensors position. Measurement origin is the leading edge of the model.

Kulite	1	2	3	4	5	6	7
$\frac{X}{L}$	0.79	0.87	1.07	1.09	1.10	1.12	1.25

**Fig. 4** 3D view of the model (Kulites in red, PCB in grey)

sors, signal amplification and galvanic insulation is done through ENS E300 signal amplifier/conditioner (with a low-pass analog filter set to 100kHz), the signal is then digitized by a NI PXIe-6358 (set to a sampling frequency of 1.1MHz). The sensors are connected to a common power supply (ITI QL355) delivering a constant 10V voltage. The uncertainty on the Kulite sensors measurements after in house static calibration by the metrology lab is less than  $\pm(15\text{Pa}+0.1\%)$  in the calibration conditions. The PXIe-6376 and PXIe-6358 are in the same PXI rack in order to use a common reference clock. The data obtained with the chosen sampling frequencies (*i.e.*, 1.1 and 3.3MHz) have been compared to data acquired at 40MHz using a Keysight Infiniium S-series numerical oscilloscope to ensure the absence of aliasing in the signal. The reference pressure for all the differential measurements (PSI and Kulite sensors) is maintained to a stable value using a vacuum pump connected to a DPI 510 pressure regulator maintaining a buffer tank of approximately 1 liter to the desired pressure (6kPa). The pressure fluctuation amplitude of the reference tank during trial runs has been measured to be less than 10Pa. To distinguish electronic noise from actual signal during the runs, reference measurements are recorded before each run (test section at vacuum pressure, wind-tunnel ready to run). This acquisition provides the noise floor.

**Table 4** Isotan thermal characteristics evaluated by the LNE.

T (K)	Diffusivity ( $10^{-6}.m^2.s^{-1}$ )	Conductivity ( $W.m^{-1}.K^{-1}$ )	Effusivity ( $W.m^{-2}.K^{-1}.s^{0.5}$ )
296	$6.00 \pm 0.3$	$21.7 \pm 1.3$	$8846 \pm 619$
323	$6.22 \pm 0.3$	$23.2 \pm 1.4$	$9287 \pm 650$

### 2.3 IR thermography setup and post-processing

To perform the heat flux measurements, a mid-wave (2.5 – 5 $\mu\text{m}$ ) FLIR SC7600 InSb (640  $\times$  512 pixels) infrared (IR) camera equipped with a 25mm lens was used. The camera is installed in the wind tunnel test section inside a specific enclosure to maintain it at atmospheric pressure and to provide sufficient cooling of the device through fresh air incoming. The use of a tilted silicon window, with a surface treatment ensuring 95% of transmittivity, eliminates the Narcisse effect. The camera is looking at the model through an aluminum mirror of optical quality as seen in figure 5 due to limited space inside the test section. To account for the experimental conditions, and more particularly for the different optics in between the camera and the model, an in-situ calibration was carried out. This operation was performed by placing a thermo-regulated heating plate (coated with the same paint as the model) inside the test section and performing camera acquisitions for different temperatures along the dynamic of interest 20 – 75°C. The derived calibration law is applied to the camera digital levels for the following measurements.

The model made of Isotan is coated with a thin layer of Sacotherm paint. Isotan thermal properties are provided in 4. The paint emissivity, together with the material has been characterized by the French National Laboratory of Tests and Metrology (LNE) for different angle of observation. At normal incidence, the paint emissivity is equal to 0.85.

Image registration and heat flux computation are described in more details in Le Sant (2005) and Le Sant et al. (2002) respectively. Therefore, only the main steps of the process will be presented in the following.

First, the model is meshed using a triangular tessellation. The camera point of view is then determined by fitting the mesh to the model contour on the image. This allows to link each pixel to a point on the model and thus to a position in space.

Secondly, camera digital levels are converted to temperature values thanks to Planck's law corrected with the emissivity value. Because each pixel can be related to its 3D coordinates on the model, the observation angle is known. The corresponding emissivity value determined by the LNE can then be applied as presented in

Le Sant (2005). The paint emissivity not been characterized for angles greater than  $60^\circ$ , it seems preferable not to consider those measurements. Consequently, the corresponding pixels are dismissed in the following.

Then, the heat flux is computed using the temperature history and the FLUX1D approach (Le Sant et al., 2002). This method solves the one-dimensional heat equation taking into account the thickness of the model, its thermal properties depending on the temperature and the thin layer of paint, which acts as a thermal resistance. The ability to take into account the model thickness is crucial in this experiment as the thermal signal depth penetration ( $\sqrt{\alpha t} = 11.7\text{mm}$ , with  $\alpha$  the thermal diffusivity of the material) is greater than the model thickness ( $7\text{mm}$ ) during a run. To do so, we consider a zero flux condition on the opposite face of the model. The impact of the curvature has been evaluated to be below 1% and consequently this effect has not been taken into account in the heat flux processing. The non-dimensional Stanton number is then computed following the relation:

$$S_t = \frac{\Phi}{\rho_\infty V_\infty C_p (T_{aw} - T_{wall})}. \quad (1)$$

Where  $\Phi$  is the heat flux determined from IR measurements,  $\rho_\infty$  is the free-stream static density,  $V_\infty$  stands for the free-stream velocity,  $C_p$  represents the specific heat at constant pressure,  $T_{aw}$  represents the instantaneous adiabatic wall temperature and  $T_{wall}$  is the model temperature measured by the IR camera. Here, the adiabatic wall temperature is inferred from static temperature  $T_\infty$  (deduced from the stagnation temperature  $T_{st}$ ) and using a turbulent recovery factor  $r \sim Pr^{1/3} \sim 0.89$ , which introduce a bias of 4.5% in laminar regions where  $r \sim Pr^{1/2} \sim 0.85$ , using the following relation:

$$T_{aw} = T_\infty \left(1 + r \frac{\gamma - 1}{2} M^2\right). \quad (2)$$

Since we investigate the instantaneous Stanton number evolution in the following, free-stream quantities are computed using the free-stream Mach number and the instantaneous stagnation pressure and temperature measured in the wind tunnel.

Finally, Stanton number distribution maps are re-projected on the 3D model thanks to the image mapping technique. An example of the resulting image is presented in figure 6. This image represents the spatial distribution of the mean Stanton number on the model. The red dots correspond to the PCB sensors. Streaky patterns are particularly visible in the reattachment region on the flare. To better recognize this striation pattern, the reader is invited to watch the movie captured

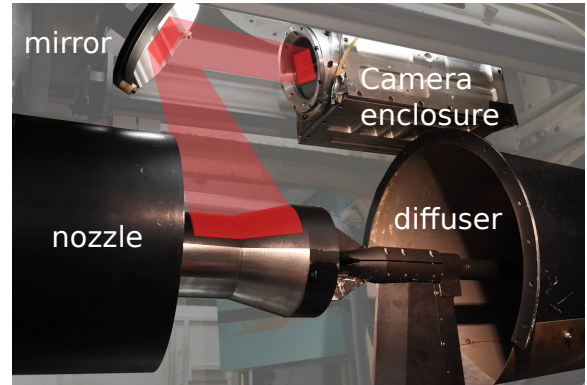


**Fig. 5** Infrared imaging setup in the R2Ch facility showing the camera enclosure, the mirror and the optical path.

by the IR camera provided in the supplementary material. From our analysis, the whole heat flux assessment uncertainties are driven by the uncertainties on the thermal properties of the material and the estimation of the paint factor. The uncertainty on the paint thermal resistivity introduces a random error of  $\pm 2.5\%$  and the one on the thermal properties of the model induce a bias ( $\pm 4\%$ ), both of those uncertainties are common to all the runs and therefore do not affect the analysis from run to run. The total uncertainty on the IR measurements is estimated to be  $\pm 6.5\%$ . The uncertainty on the recovery factor lead to an estimated uncertainty on the Stanton number of  $+11\% - 6.5\%$ .

Unless specified otherwise, no spatial nor temporal averaging or filtering of the IR data is conducted.

Figure 6 indicates the two valid areas seen by the IR camera: the IR image represents the low-frequency acquisition (50Hz) which covers both the cylinder part of the model and the full flare; in red, the high-frequency acquisition (972Hz) which focuses on a reduced region at the beginning of the flare. In both cases, the corresponding spatial resolution provided by the camera is  $0.4\text{mm}/\text{pixel}$ . IR acquisitions were triggered manually to record the full temperature history during the wind tunnel blow-down as indicated in figure 3.

A cylindrical coordinate system will be used, as it allows to better represent the axisymmetrical geometry and flow. The cylindrical coordinate system is derived from the Cartesian presented in figure 6,  $x$  is kept the same with an origin at the leading edge of the model. The radius  $r$  is defined as  $r = \sqrt{y^2 + z^2}$  ( $y$  and  $z$  origin are located on the symmetry axis of the model) and the angle  $\theta$  as  $\theta = \tan^{-1}\left(\frac{z}{y}\right) + 90$ ,  $\theta$  is defined in degrees.

To extract information about the azimuthal striation from the IR images, an azimuthal decomposition consisting of the following steps is used. First, the  $N_i$  images are interpolated on a regular  $(x, \theta)$  grid. Then, a Discrete Fourier Transform (DFT) is applied in the az-

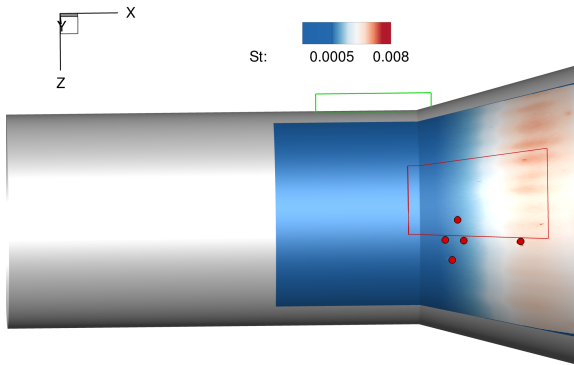


**Fig. 6** Part of the model filmed by the infrared camera in the  $50Hz$   $640 \times 512$  full frame case (a mean Stanton number map is displayed as an example) and  $972Hz$   $208 \times 88$  reduced frame case (red line). The green box represents the area filmed by the Schlieren imaging setup (see next section).

imuthal direction, giving Fourier mode vectors  $\hat{\mathbf{S}}^k(m)$ , where  $k$  is the image number and  $m$  the azimuthal wavenumber of the mode. It is important to note here that the DFT cannot be computed at the longitudinal location of the PCB sensor due to their presence in the IR images. Due to the spectral transformation in the azimuthal direction, the vectors  $\hat{\mathbf{S}}^k(m)$  correspond to mono-dimensional vectors of pixels: they contain complex values associated with the pixel intensity at each point ( $x$ ) from the mesh. For a given wavenumber ( $m$ ) of interest, the Fourier modes of all the images are then stacked in a matrix  $\hat{\mathbf{X}}_m$ , which reads

$$\hat{\mathbf{X}}_m = \left[ \hat{\mathbf{S}}^0(m), \hat{\mathbf{S}}^1(m), \dots, \hat{\mathbf{S}}^{N_i-1}(m) \right]. \quad (3)$$

This matrix is then processed similarly to a snapshot matrix in a classical POD decomposition: the  $i$ -th POD mode  $\phi_i^{(m)}$  can be computed from the  $i$ -th left singular vector of  $\hat{\mathbf{X}}_m$ , which may be computed by solving the eigenproblem associated with the cross-spectral density matrix

$$\hat{\mathbf{X}}_m \hat{\mathbf{X}}_m^* \psi_i^{(m)} = \lambda_i^{(m)} \psi_i^{(m)}, \quad (4)$$

For each wavenumber ( $m$ ), the associated POD modes are ordered with respect to their contribution to the global dynamics, *i.e.*  $\lambda_0^{(m)} > \lambda_1^{(m)} > \lambda_2^{(m)} > \dots$

In practice, the eigenmodes are computed by using the snapshots method of Sirovich (1987) which is a less costly but equivalent decomposition based on

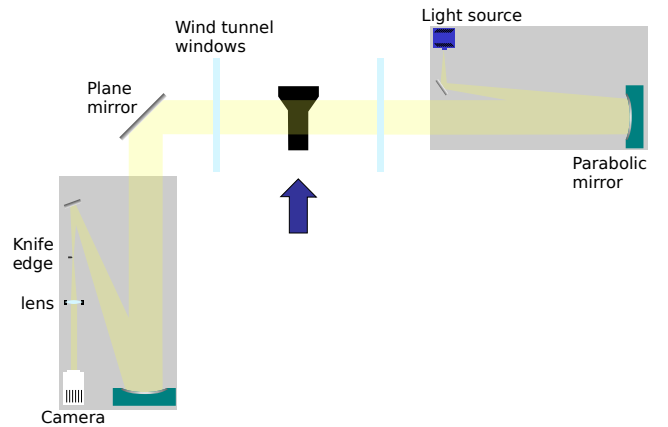


**Fig. 7** Schematic of the Schlieren setup.

$\hat{\mathbf{X}}_m^* \hat{\mathbf{X}}_m$  rather than (4). This provides the right singular vectors of  $\hat{\mathbf{X}}_m$ , from which one can easily retrieve the POD modes (see for instance Towne et al. (2018) for details). While for traditional POD, multiple modes are needed to describe the data, here the POD comes after a DFT, giving a different set of modes per wavenumber of interest. In this article, the POD is mainly used to discriminate the correlated physical information at a given frequency from the uncorrelated noise coming from the environment or the acquisition. As such, only the leading mode will be presented and discussed for the wavenumber of interest.

## 2.4 Schlieren setup and images treatment

Flow visualizations were realized thanks to the classical Z-type Schlieren setup presented in figure 7. Due to environmental constraints, the reception side has been folded using a large plane mirror. In conjunction with a HBO arc-lamp, a Phantom V2640 high-speed camera was employed to investigate the recirculation region close to the flare junction. The camera was operated at  $140kHz$ , on a reduced region of  $752 \times 128$  pixels depicted in figure 6. The knife edge was set horizontally to visualize vertical density variations in the shear layer.

A typical image recorded with the high-speed camera setup is presented in figure 8. While it clearly displays the density gradient of the mixing layer, it is harder to identify structures linked with unsteady features of the flow in this image. One may nonetheless note the presence of alternating zones of low/high density gradient within the shear layer. The reader is invited to watch the movie provided in the supplementary material to better distinguish those structures. No spatial nor temporal averaging or filtering of the Schlieren data is conducted.



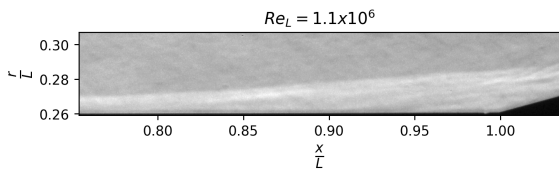


**Fig. 8** Example of instantaneous Schlieren images from the dataset used for the SPOD.

To extract information on those potentially spatio-temporally correlated structures, Spectral Proper Orthogonal Decomposition (SPOD) is used. This variant of the classical Proper Orthogonal Decomposition (POD) was first introduced by Lumley (1970) and has been widely used by the turbulence community since then (see for instance Gudmundsson and Colonius (2011)). It has been recently studied from a mathematical point of view by Towne et al. (2018), who showed that it is by construction the optimal decomposition to identify spatio-temporally correlated structures within statistically stationary flow. Recently, it has been used with great success to post-process high-speed Schlieren images in hypersonic wind tunnel experiments (Butler and Laurence, 2021a,b).

The actual treatment is done following a procedure that is close to the one used for the IR post-processing but includes a temporal Fourier transform instead of a spatial one : First, the instantaneous images are re-grouped in  $N_r$  overlapping realizations of the flow. Each realization contains a temporal sequence of vectors representing the images ( $\mathbf{s}_{t_0}, \mathbf{s}_{t_0+\Delta t}, \dots$ ), where the components of  $\mathbf{s}_t$  are the intensity of the pixels of the 2D image at the time  $t$ . A Discrete Fourier Transform (DFT) is then applied in the temporal direction, giving Fourier mode vectors  $\hat{\mathbf{S}}^k(\omega)$ , where  $k$  is the realization number,  $\omega$  the temporal frequency. For a given frequency  $\omega$  of interest, the Fourier modes of all realizations are then stacked in a matrix  $\hat{\mathbf{X}}_\omega$ , which is then treated following the same procedure described here-before for  $\hat{\mathbf{X}}_m$  in the case of the IR post-processing (the matrix is decomposed by POD). Due to the prior temporal DFT, this processing yields a set of oscillating mode structures for each temporal frequency. The numerical parameters such as the number of images, the realization size and the number of realizations are presented in table 5. Again, only the leading SPOD mode (and its energetic content) will be presented and discussed for each frequency of interest.

Sampling rate	140 kHz
Number of images	83324
Number of images in each realization	2048
Frequency resolution	68Hz
$N_r$	80

**Table 5** Numerical parameters for the SPOD.

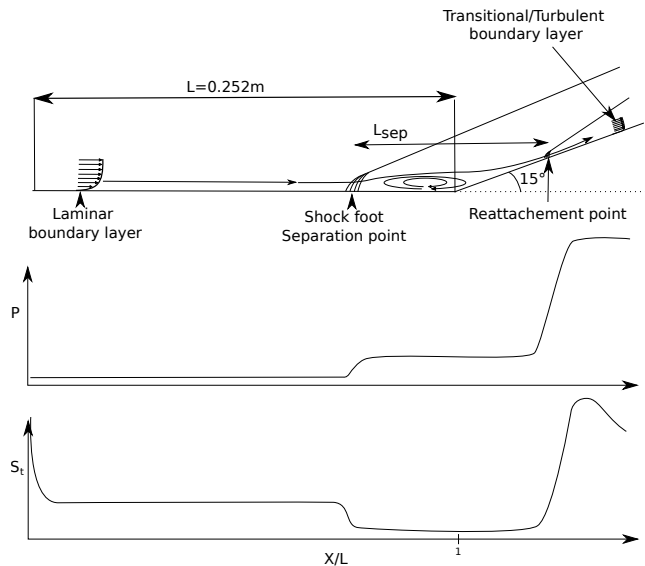


**Fig. 9** Schematic of a strongly separated SBLI on the compression ramp under study (top) of the typical wall pressure distribution along the geometry (middle) and Stanton number distribution (bottom).

### 3 Results

#### 3.1 Flow topology

Let us first document the impact of the Reynolds number on the topology of the flow, and particularly on the recirculation region size. Figure 9 presents a schematic of the flow topology showing the separation shock, the recirculation region, the reattachment and an illustration of the typical pressure and Stanton number evolution through those regions. As the flow on this exact setup is already described in depth by Benay et al. (2006), only the information relevant to the present study will be presented in this section. Figure 10 presents the main indicators of the change in flow topology: time averaged wall pressure (a) and normalized pressure (b) distributions and mean (time and azimuthal average) heat-fluxes represented by Stanton number evolution along the model (c). As already documented by Benay et al. (2006) for a broad range of Reynolds numbers, the topology of the flow is strongly impacted by the Reynolds number change. First, the recirculation bubble, which is characterized by the pressure plateau after the first pressure rise, decreases in size while increas-



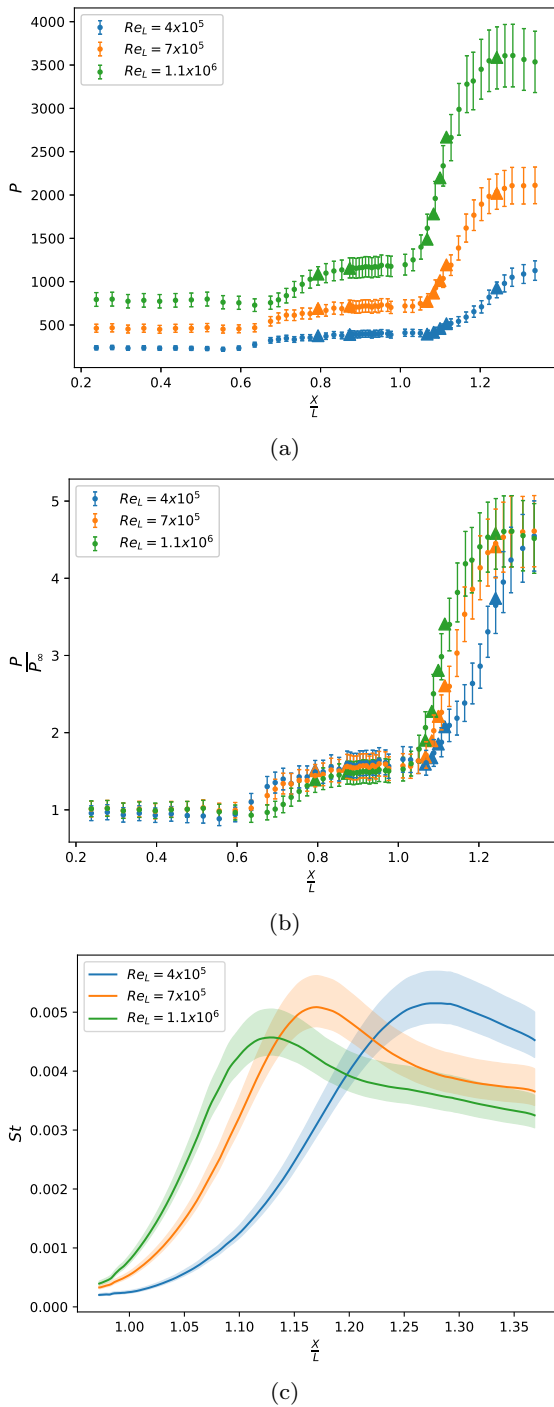


**Fig. 10** Topology of the flow described by the mean (averaged on 2-second windows during the high-speed acquisition) wall pressure distributions (a) and normalized ( $P_\infty$  is the free-stream static pressure) pressure distribution (b) the small dots are measurements from the pressure scanner while the big triangles are from Kulites sensors. Mean Stanton number evolution computed as the temporal (averaged on 2-second windows during the high-speed acquisition) and azimuthal average of the Stanton number (c).

ing the Reynolds number. The impact of the Reynolds number on the recirculation region size was also documented by Heffner et al. (1993) on a similar configuration. This reduction happens with both a downstream displacement of the separation point and an upstream displacement of the reattachment point. The upstream displacement of the separation point is well illustrated by figure 10(a) as the pressure rise caused by the separation happens sooner for lower Reynolds number. The downstream displacement of the reattachment point can be inferred from figure 10(c) and previous observation from Heffner et al. (1993), which have shown that the reattachment point position is located near the peak heat-flux position in transitional SBLI (according to Running et al. (2020) it is actually just upstream of the peak). The peak heat flux position is very clearly displaced downstream by a decrease in Reynolds number in the present experiments. Similar behavior of the separated region has also been documented numerically, albeit for increasing free-stream perturbations instead of Reynolds number, both for incompressible separated region (Marxen and Rist, 2010) and hypersonic SBLI separated region (Lugrin et al., 2021b), showing that the transitional instabilities play an important role in the definition of the recirculation region size. Here, the same mechanisms could be at play, with transitional instabilities strengthened by the increase in Reynolds number instead of the increase in amplitude of the injected perturbations.

For all the cases presented here, the heat-flux peaks at a higher value than in the turbulent regime, which is typical of transitional flows. The transitional peak Stanton values on the flare, in the 10–25% higher than the turbulent Stanton value range, compares well with other experimental and numerical results (see for instance Heffner et al. (1993); Benay et al. (2006); Navarro-Martinez and Tutty (2005); Vermeulen and Simeonides (1992)). The peak Stanton value of  $St \sim 5 \times 10^{-3}$  is also coherent with the previous results of Benay et al. (2006). The displacement of the reattachment point and thus of the maximal heat-flux location is also illustrated by the heat-flux maps presented in figure 11.

The evolution of state of the boundary layer on the flare for each case can be deduced from the results of figure 10; For the  $Re_L = 4 \times 10^5$  case, at the end of the flare, the Stanton peak caused by transition is not over, meaning that the flow does not reach a fully turbulent state on the flare, and as such, the transition process is not fully over. For the two other cases, the Stanton number decreases after the transitional peak and reaches a steadily decreasing plateau on the flare, sign that the flow reaches a fully turbulent state.

It is worth to mention here that no clear evidence of SBLI unsteadiness was found in the present experiment, neither on full frame Schlieren imaging nor on the spectrums of pressure transducers located inside the bubble. Either there is not any low-frequency separated region motion or a very low amplitude one. The SBLI unsteadiness is also known to have a negligible impact on the transition process in noisy environment (Lugin et al., 2021a).

The next sections focus on the streaky pattern in the reattachment and the shear layer modes, on which the literature is more sparse.

### 3.2 Streaks analysis

As stated in the introduction, heat-flux striation is common in the reattachment region of SBLI and the origin of this phenomenon is under debate.

The first interesting information to extract from the infrared images is the wavenumbers associated with the streaks and how it depends on the Reynolds number. Looking at figure 11 already provides qualitative information on the dominant wavenumbers of the streaks. The overall wavelength of the streaks seems to be decreasing along the intensity of the striation with an increase in the Reynolds number. A similar trend was already described for laminar hypersonic SWBLI by Aymer De La Chevalerie et al. (1997) as they noted a shift from high-amplitude/low-wavelength toward moderate amplitude and wavelength patterns with an increase in the Reynolds number. This trend was also observed by Running et al. (2020). Then, similarly to what was reported by Running et al. (2020), some peaks and valleys are amplified more than others, which may suggest that there is either an uneven receptivity of the streaks or that multiple modes at different wavenumber may be superposed. As the streaks break down and the flow become turbulent on the flare, the heat-flux striation become less visible on the mean Stanton map and is replaced by a uniform heat-flux distribution. Because of that, the length of the clearly striated region is Reynolds-number-dependent: for the low Reynolds number case, the transition process is not over at the end of the ramp, and thus the streaks are clearly visible from the reattachment point to the end of the model. For the higher Reynolds number cases, the streaks breakdown to turbulence quickly and cause striation to be clearly visible only on a small axial part of the model near the reattachment point. A similar behavior was also observed for transitional cases by Vermeulen and Simeonides (1992) and by Roghelia et al. (2017) for increasing ramp angle. As postulated by Vermeulen and Simeonides (1992) this suggests that the

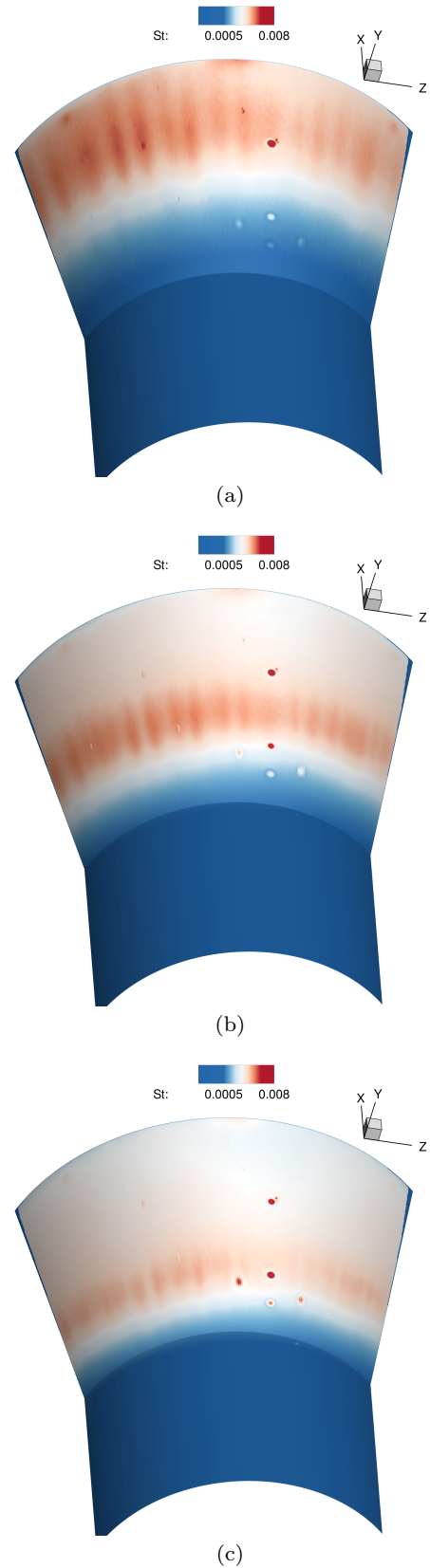


**Fig. 11** Mean (time average of the images) Stanton number distribution from infrared imaging for (a)  $Re_L = 4 \times 10^5$ , (b)  $Re_L = 7 \times 10^5$ , (c)  $Re_L = 1.1 \times 10^6$ . To improve the rendering of the 3D geometry, the Tecplot lighting effect is used.

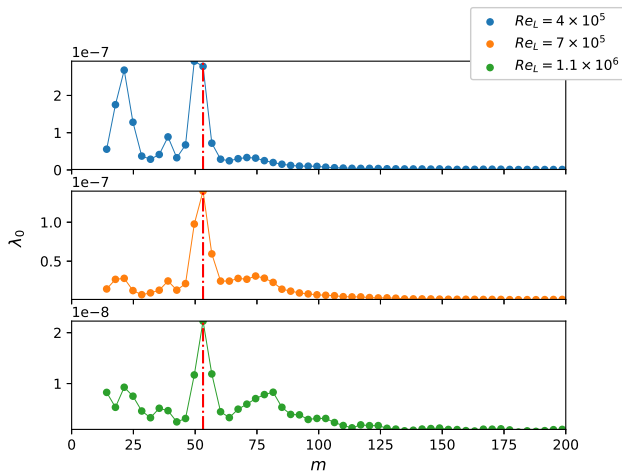


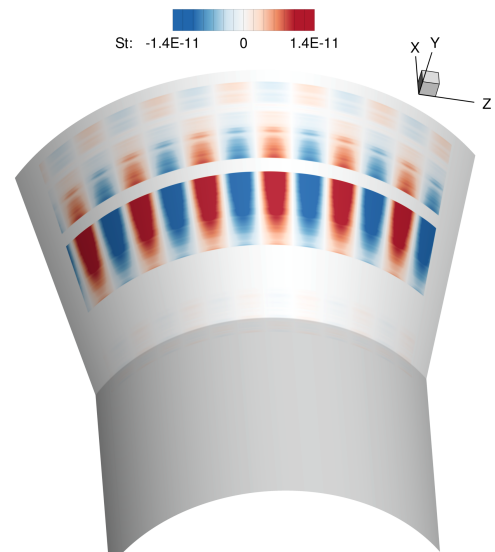
**Fig. 12** Energetic content of the streaky pattern against wavenumber for each Reynolds number. Computed from the azimuthal Fourier decomposition of infrared images followed by POD (see 2.3).

streaks are involved in the transition process. It is important to mention here that the absence of striation on the flare is not a good indicator of the turbulent state of the boundary layer in that region, given that laminar reattachment with no striation has also been documented (Benitez et al., 2021).

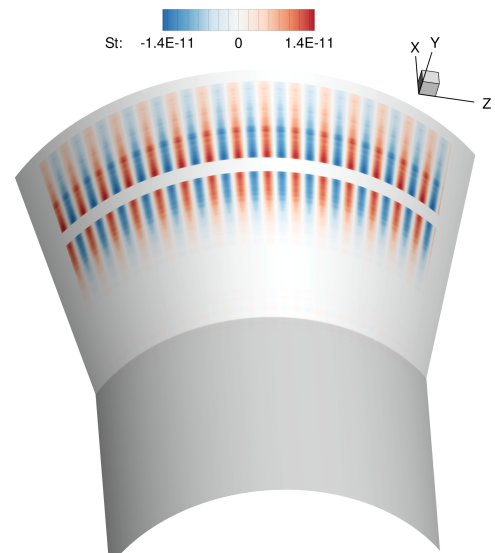
To get quantitative information on the dominant wavelength of the streaks, one can follow the procedure described in section 2.3 to post-process the instantaneous IR images (see the movie in the supplementary materials).

Figure 12 presents the energy of the leading POD mode as a function of the azimuthal wavenumber  $m$  for each Reynolds number. The interpretation of the absolute value of  $\lambda_0$  presented in this figure is subject to caution. The azimuthal decomposition cannot be computed in regions where discontinuities are present. Consequently, azimuthal slices of the images containing PCB sensors have to be masked (see figure 13 for instance), leading to an underestimation of the total energy of the mode. As the reattachment region position depends on the Reynolds number, the missing energy from the masked part will not be the same for all Reynolds numbers (for instance, the maximum peak heat flux may be masked for the high Reynolds number case and not for the others).

First, there are multiple peaks in the spectra, highlighting that there may be multiple different mechanisms leading to the apparition of streaks. This is consistent with the previous observation of uneven striation on the flare, which may be due to the superposition of different modes.



(a)



(b)

**Fig. 13** Reconstructed POD mode from the most energetic modes at  $Re_L = 4 \times 10^5$  (a)  $m = 21$  and (b)  $m = 53$ . The masked bands correspond to region where the presence of PCB sensors makes the computation of the azimuthal Fourier decomposition impossible. The amplitude of the mode is arbitrary. To improve the rendering of the 3D geometry, the Tecplot lighting effect is used.

The first peak, at  $m = 21$  is only present (and dominant) in the low Reynolds number flow. This peak disappears when the Reynolds number increases. Another highly energetic peak is present at  $m = 53$  for all the studied cases. The wavenumber of this peak is completely independent of the Reynolds number (and thus of the size of the separated region). Finally, a third energetic zone appears with the increase of the Reynolds number for a large range of wavenumbers

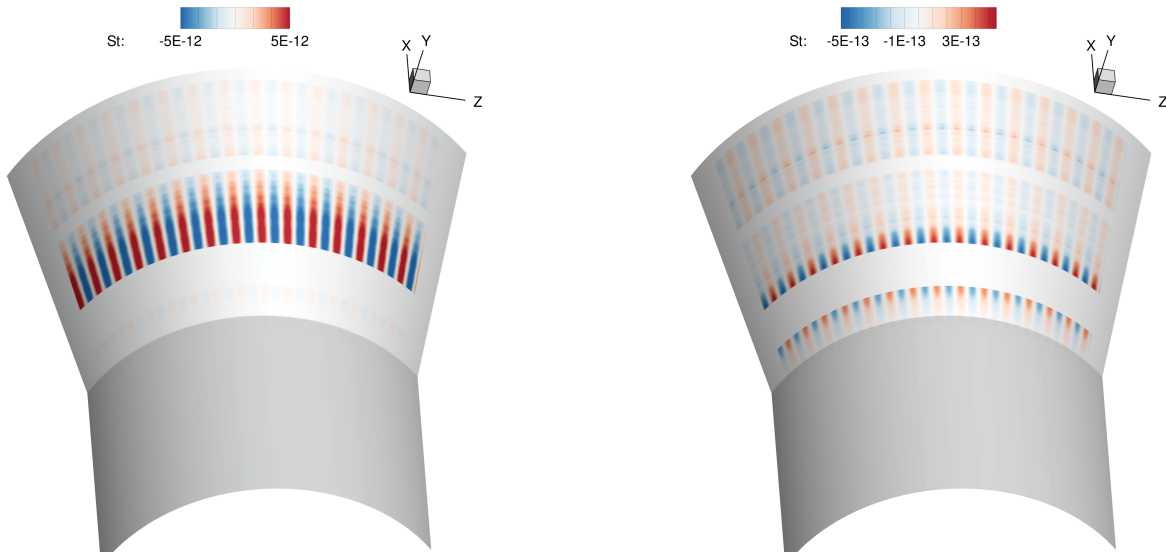


**Fig. 14** Reconstructed POD mode from the most energetic mods at  $Re_L = 7 \times 10^5$  ( $m = 53$ ). The masked bands correspond to region where the presence of PCB sensors makes the computation of the azimuthal Fourier decomposition impossible. The amplitude of the mode is arbitrary. To improve the rendering of the 3D geometry, the Tecplot lighting effect is used.

around  $m = 81$ , which becomes more and more significant when the Reynolds number increases.

Thus, three different peaks have been identified in figure 12 and should be studied. Those peaks may be linked with different physical mechanisms. Figures 13, 14, and 15 present the azimuthally reconstructed leading POD mode ( $\psi_i^{(m)} e^{im\theta}$ ) at the dominant wavenumbers for each Reynolds number, which provide information on the spatial organisation of the modes.

First, the striation pattern at  $m = 21$  is displayed in figure 13 (a) as it is only present for the lowest Reynolds number case. It displays a streamwise change in the heat flux sign in addition to the obvious azimuthal one. The region of positive heat flux variation at reattachment is followed by a region of negative variation on the edge of the flare. Hildebrand et al. (2018); Lugin et al. (2021a) showed in their numerical work that global unstable modes in the recirculation region of transitional hypersonic SBLI could lead to such an alternate pattern in the streamwise direction. Neither Görtler instabilities nor other convective mechanisms such as unveiled by Dwivedi et al. (2019) display such streamwise pattern. Therefore, it is possible that the mode at  $m = 21$  is caused by such a global mode and it appears unlikely that those streaks are caused by convective mechanisms.

For the  $m = 53$  pattern, which is presented in figures 13 (b), 14 and 15 (a) (as it is present for all Reynolds

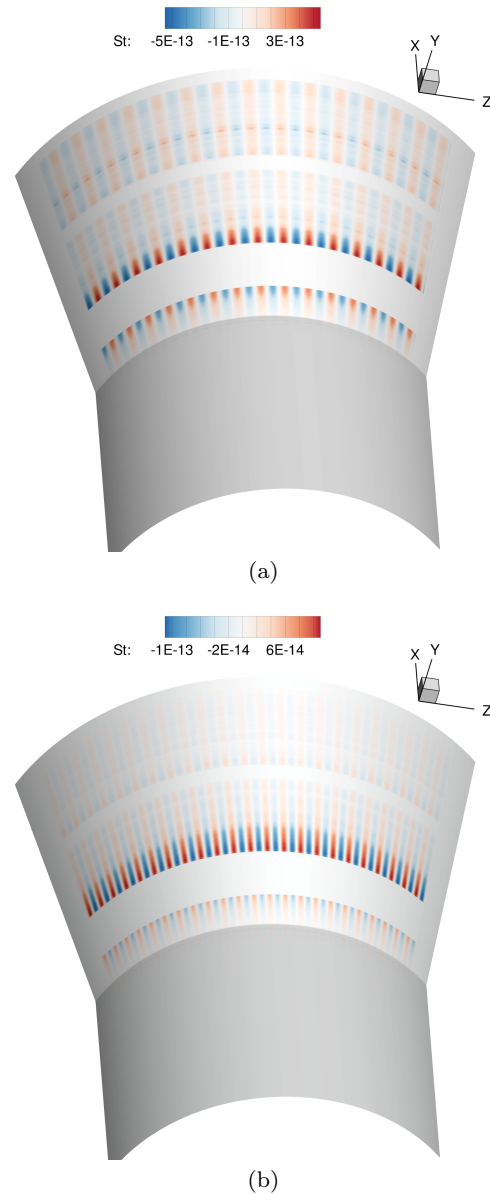


**Fig. 15** Reconstructed POD mode from the most energetic modes at  $Re_L = 1.1 \times 10^6$  (a)  $m = 53$  and (b)  $m = 81$ . The masked bands correspond to region where the presence of PCB sensors makes the computation of the azimuthal Fourier decomposition impossible. To improve the rendering of the 3D geometry, the Tecplot lighting effect is used.

number), the streamwise pattern completely disappears, hinting that this mode may not be linked with the same physics. striation pattern appears similar to the one presented by Dwivedi et al. (2019) and Lugin et al. (2021b). As such the mode at  $m = 53$  could be linked to convective mechanisms. However, Cao et al. (2021) proved that non-linear saturation of unstable global modes could also lead to streaks which do not display any alternate pattern past reattachment. While both of those mechanisms could lead to a similar striation pat-



tern, they should be impacted by a change in Reynolds number and are thus unlikely to be at the origin of this striation. The hypothesis that they could be caused by a centrifugal mechanism such as initially proposed by Benay et al. (2006) is the most relevant in that case, as Görtler vortices can be extremely receptive to leading edge geometrical imperfection (Vermeulen and Simeonides, 1992; Roghelia et al., 2017) which could explain why the wavenumber is not  $Re_L$ -dependent.

For the third amplification at high wavenumber ( $m \sim 81$ ), the dominant mode at  $m = 81$  for  $Re_L = 1.1 \times 10^5$  is presented in figure 15 (b); Again, it does not display any longitudinal pattern. There are two hints that point toward a purely convective mode such as described by Dwivedi et al. (2019): first, it displays energetic content over a wide range of wavenumber (which is often the case for convective modes that act as noise amplifiers (Sipp and Marquet, 2013)) and second, it seems to be more and more dominant when increasing the Reynolds number.

Traces of the  $m = 53$  and  $m = 81$  modes are still visible even in the fully turbulent region on the flare even if their amplitude in that region is way less than in the transitional region (which may explain why they were not visible on the mean Stanton number map presented in figure 11). This result is reminiscent of previous numerical results (Lugrin et al., 2021b) which have shown that such coherent structures are indeed still present even in fully developed turbulence past the transitional reattachment point.

Now that the dominant modes linked with streaks are identified, their temporal behavior can be characterized. To get that information, IR imaging was conducted on a reduced part of the model at higher sampling frequencies (972Hz, see section 2.3). Figure 16 presents the temporal evolution of the flux along an azimuthal line located at the streamwise location associated with the peak mean heat-flux for all 3 runs. Following the work of Running et al. (2020), a detrending is conducted by subtracting a linear best-fit of the data (in the azimuthal direction). This allows to get rid of both the mean and potential very-low wavenumber signal that would complicate the detection of the streaks' centerlines. For each figure, the signature of the dominant streaks ( $m = 53$ ) is visible (the centerline of high-heat flux streaks are indicated by a dashed line, the waveangle of around  $7^\circ$  correspond to a wavenumber of  $\frac{360}{7} \sim 51$  very close to 53), this signature is not constant in time but seems to be meandering. While the time resolution is not sufficient to accurately describe the full motion of the streaks, one may already draw interesting conclusions from that. First, the streaks are not steady. However, their unsteadiness is somewhat

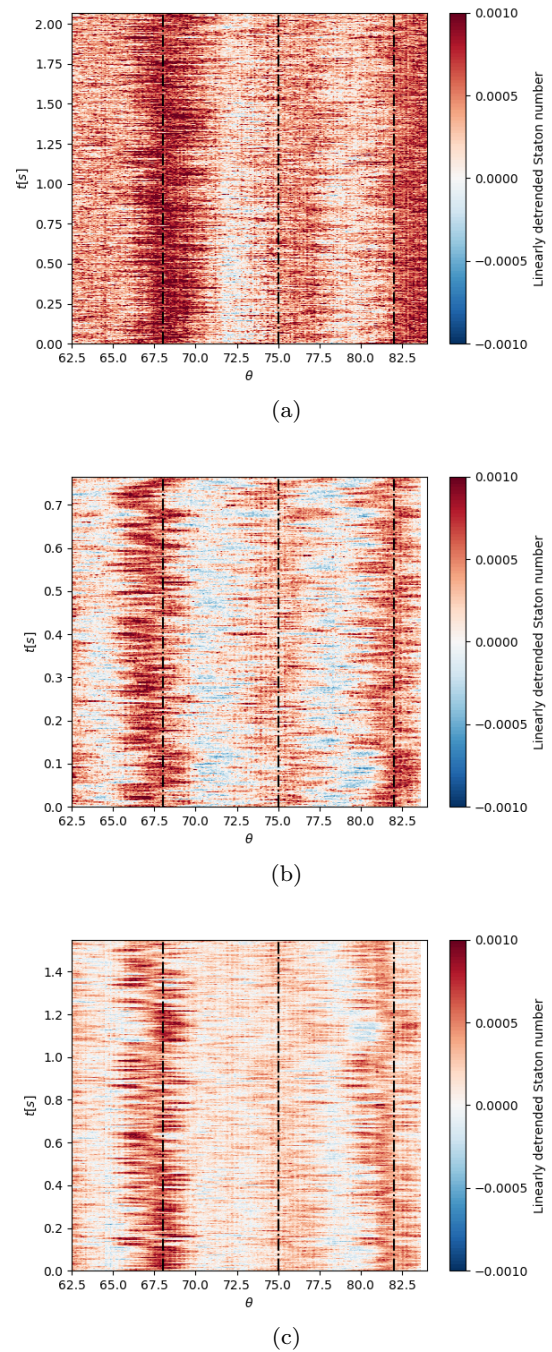


**Fig. 16** Time evolution of azimuthal Stanton number distribution measured with the infrared camera at 972Hz at  $Re_L = 4 \times 10^5$  (a),  $Re_L = 7 \times 10^5$  (b) and  $Re_L = 1.1 \times 10^6$  (c). The dashed lines represent the centerline of high-heat flux streaks. The  $t = 0$  time correspond to an arbitrary time reference once the flow is fully started.



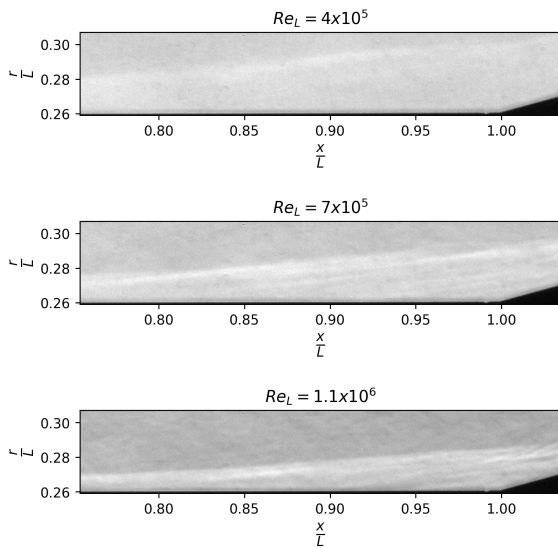


**Fig. 17** Instantaneous Schlieren images.

limited, as they seem to be moving only slightly around their mean position. They are neither rotating nor entirely changing position. This leads to similar (but improved) conclusions compared to those obtained by [Benay et al. \(2006\)](#); while they were right about the presence of quasi-steady streaky pattern on the flare, their oil flow visualization technique was unable to reveal the small unsteadiness around the mean position measured here. [Running and Juliano \(2021\)](#) also came to the same conclusion from unsteady PSP data. Another interesting information brought by the comparison of figure 16 (a), (b) and (c) is that the centerline of the  $m = 53$  streaks is run and  $Re_L$ -independent, which can only reinforce the hypothesis that they are linked with receptivity of geometrical imperfection of the model.

To summarize, this study has unveiled the presence of different types of striation patterns on the flare. It points towards multiple mechanisms at play in the creation of streaks. Some evidences seem to indicate that at least one of the mechanism is linked with a global unstable mode. There are also signs of the presence of convective amplification mechanisms and Görtler vortices.

### 3.3 Shear-layer oblique modes

The last important features of the flow under study are the structures in the shear layer which are visible in the Schlieren images presented in figure 17 and the movie provided in the supplementary materials. The images are hard to interpret directly, since the weak density of the flow leads to very low contrast. However, one may still see what looks like travelling structures in the

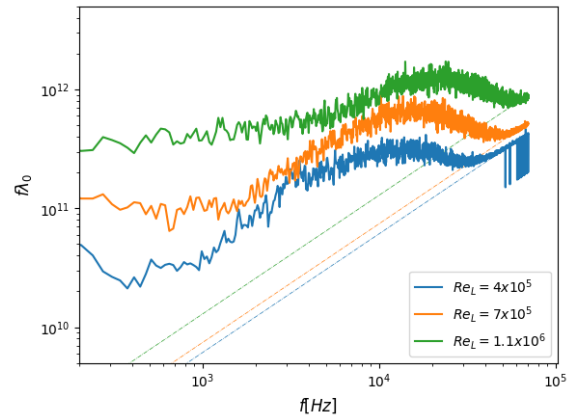


**Fig. 18** Pre-multiplied energy level  $\lambda_0$  of the leading SPOD mode against frequency for all the Reynolds numbers. The dashed lines correspond to the noise floor of the camera.

shear layer, which could be studied using SPOD. Note that compared to two-dimensional studies, the present axisymmetric model minimizes the integration effect of the Schlieren measurement and thus the spatial averaging of shear layer structures. Figure 18 shows the pre-multiplied energy content of the SPOD leading mode against frequency. The noise floor of the camera (which is constant with frequency) is displayed as a dotted line for each run. It shows that the increase in energy in the last part of the pre-multiplied spectrums is only due to this constant noise floor. This information allows us to conclude that no physics can be captured with those settings at a frequency higher than 70kHz (the motion blur caused by the  $1\mu\text{s}$  exposure time acts as a low pass filters) and that the spectrums are free of aliasing. The spectrums display broad bumps that span over more than  $\sim 10\text{kHz}$ , with frequencies increasing with the Reynolds number.

The leading modes associated with the maximum energy of those bumps are presented in figure 19. For every case, the leading mode displays alternating structures located in the shear layer on top of the bubble. When the Reynolds number increases, and as the frequency increases too, the longitudinal wavelength of the mode decreases. From the SPOD results, one can make several hypotheses about the physics of this mode. First, the broad bump in the spectrums indicates that they originate from a convective mechanism and are subject to receptivity. From there, and given their localization in the shear layer they may be compressible oblique supersonic shear-layer instabilities, which are well documented in the numerical literature ([Sandham and Reynolds, 1990](#); [Kudryavtsev and Khotyanovsky, 2005](#); [Foysi and Sarkar, 2010](#)). The frequency range of those instabilities is consistent with the numerical results from [Lugin et al. \(2021b\)](#) who documented such

shear layer oblique convective modes in a similar flow configuration.

The leading mode also displays close to no signature in the near-wall region. So, one could expect that the pressure transducers will not be able to properly capture the dynamics of the mode.

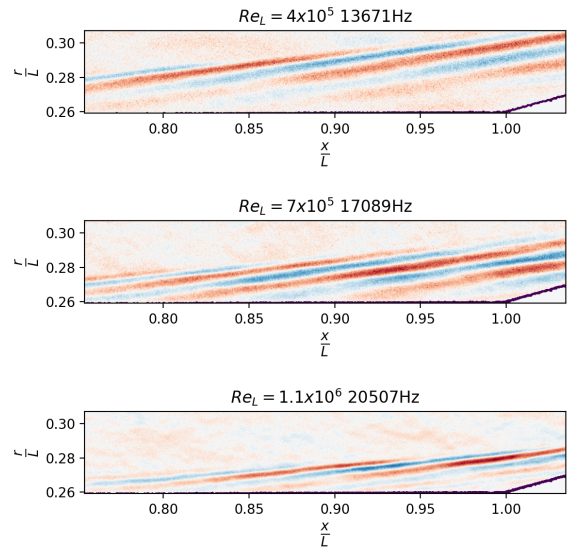
Figure 20 shows the pre-multiplied pressure power spectral densities measured by a Kulite and a PCB sensor located at the reattachment. First, the bandwidth of the Kulite sensor is very limited. The energetic content of fluctuations measured with the Kulite sensors starts to decrease before 10kHz while the one measured by the PCB is still increasing.

The PCB spectrums are broadening towards high-frequencies with increasing Reynolds number. For the  $Re_L = 4 \times 10^5$  case, the spectrum display very low level of energy in the  $f > 50kHz$  region (the signal in that region is mostly electronic noise), which is a sign that the flow is not turbulent at the location of the sensor. Meanwhile, for the two higher Reynolds number cases, the spectrums display an increasing level of energy in that frequency region, which is a sign that the flow is becoming turbulent. This result is consistent with the conclusion of section 3.1.

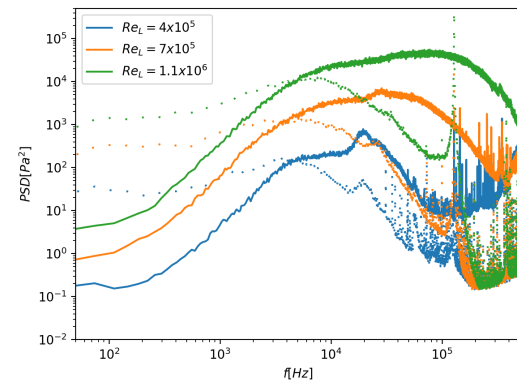
For the lowest Reynolds numbers, a large peak is visible at approximately 20kHz. It is also visible in the spectrums of the intermediate Reynolds number at a slightly higher frequency. Even if this frequency is higher than that of the oblique mode in the shear layer, this peak could be a trace of those structures as the frequency may increase at reattachment were the boundary layer is compressed (a decrease in thickness leading to an increase in frequency).

Figure 21 presents the pre-multiplied pressure power spectral density measured by a Kulite pressure transducer located inside the recirculation bubble. Given the already-discussed limited bandwidth of this sensor and the fact that the waves are traveling in the shear layer and not in the near wall region of the bubble, the interpretation of those spectrums is subject to caution. It is still interesting to note that there is a broad peak in the 1 – 10kHz range, with a frequency increasing with the Reynolds number.

The comparison with the SPOD results is not straightforward as the SPOD gives a global spectrum of the integrated energy while the sensor is more localized. Pixels near the sensors located in the bubble (the one at reattachment is not visible on the images) could have been used to compute a localized version of the Schlieren spectrums to give a good comparison. Unfortunately, the signal-to-noise ratio is extremely low in that region and the resulting spectrums are impossible to interpret. Keeping those limitations in mind, this



**Fig. 19** Most energetic leading SPOD mode linked with oblique shear layer modes for all the studied Reynolds number.



**Fig. 20** Pre-multiplied pressure power spectral density from the Kulite 3 sensor (dotted) and the PCB 1 sensor (line) on the flare for all the Reynolds numbers, showing the limited bandwidth of the Kulite sensors.

study nonetheless reveals the similarity between the Schlieren and pressure transducers spectra; the peak is in a similar frequency range and the frequency increases with Reynolds number with both techniques.

To conclude, shear layer modes were identified using Schlieren imaging. They seem to be the dominant instability in the shear layer on top of the bubble. Pressure transducers on the surface of the model appear unable to further characterize those modes, probably because the modes do not cause strong fluctuations in the near wall region.

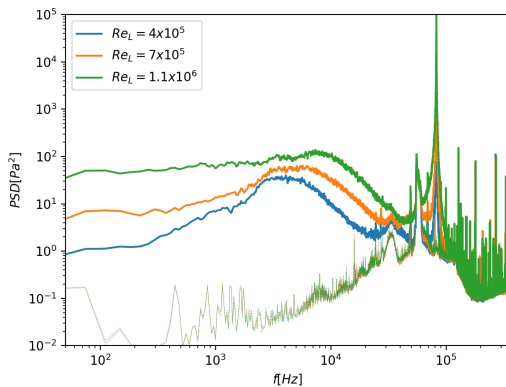


**Fig. 21** Pre-multiplied pressure power spectral density from the Kulite 2 sensor (line) and pre-run noise level (dashed) inside the recirculation region for all the Reynolds numbers.

## 4 Conclusion

Experiments were conducted in the R2Ch blowdown facility to study the transitional shockwave/boundary layer interaction on the hollow cylinder flare geometry of Benay et al. (2006) at a Mach number of 5. Means of investigation are infra-red thermography, high-speed Schlieren visualisation and pressure transducers along the model. The IR imaging showed the presence of streaks in the reattachment region at different wavenumbers. The in-depth study of those streaks and comparison with numerical results from the literature brought evidence that they are likely to originate from different physical mechanisms, either linked with global or convective linear mechanisms. To the authors' knowledge, it is the first time that a Fourier decomposition coupled with POD is conducted on IR data and that different mechanisms causing striation in the reattachment region of SBLI are identified and clearly distinguished.

Oblique shear layer modes were identified using Schlieren imaging as the dominant instability in the shear layer above the recirculation region. Those modes have a very low-pressure signature at the wall, making their identification via wall-measurements complex. The role played by streaks and shear layer modes in the transition process is still an open question, but the present study tends to show that either one of them or a combination of both may be at the origin of the transition. Precise numerical reproduction of those experiments would be necessary to accurately describe the transition process and to assess whether the constant-wavenumber streaks are due to the leading edge geometry or to a physical mechanism that is fully independent of the Reynolds number.

**Acknowledgements** This work was supported by the French Alternative Energies and Atomic Energy Commission (CEA) under the grant CEA 4600334751. The authors thank Julien Dandois for its comments on the paper as well as Jean-Marc Luysen, Pascal Audo, Gilles Peugnier, Gilles Losfeld, Cedric Illoul, Yves Le Sant and Joël Rousseau for their participation in the experimental campaign.

## Conflict of interest

The authors declare that they have no conflict of interest.

## References

- Adams NA (2000) Direct simulation of the turbulent boundary layer along a compression ramp at  $M = 3$  and  $Re(\theta) = 1685$ . *Journal of Fluid Mechanics* 420:47–83, DOI 10.1017/S002211200001257
- Aymer De La Chevalerie D, Fonteneau A, De Luca L, Cardone G (1997) Görtier-type vortices in hypersonic flows: The ramp problem. *Experimental Thermal and Fluid Science* 15(2 SPEC. ISS.):69–81, DOI 10.1016/s0894-1777(97)00051-4
- Benay R, Chanetz B, Mangin B, Vandomme L, Perraud J (2006) Shock wave/transitional boundary-layer interactions in hypersonic flow. *AIAA Journal* 44(6):1243–1254, DOI 10.2514/1.10512
- Benitez EK, Jewell JS, Schneider SP, Esquieu S (2020) Instability measurements on an axisymmetric separation bubble at mach 6. In: *Aiaa Aviation 2020 Forum*, vol 1 PartF, pp 1–29, DOI 10.2514/6.2020-3072
- Benitez EK, Jewell JS, Schneider SP (2021) Separation bubble variation due to small angles of attack for an axisymmetric model at mach 6. In: *AIAA Scitech 2021 Forum*, pp 1–23, DOI 10.2514/6.2021-0245
- Bur R, Chanetz B (2009) Experimental study on the PRE-X vehicle focusing on the transitional shock-wave/boundary-layer interactions. *Aerospace Science and Technology* 13(7):393–401, DOI 10.1016/j.ast.2009.09.002
- Butler CS, Laurence SJ (2021a) Interaction of second-mode disturbances with an incipiently separated compression-corner flow. *Journal of Fluid Mechanics* 913, DOI 10.1017/jfm.2021.91
- Butler CS, Laurence SJ (2021b) Interaction of second-mode wave packets with an axisymmetric expansion corner. *Experiments in Fluids* 62(7):1–17, DOI 10.1007/s00348-021-03235-2
- Cao S, Hao J, Klioutchnikov I, Olivier H, Wen CY (2021) Unsteady effects in a hypersonic compression ramp flow with laminar separation. *Journal of Fluid Mechanics* 912:A3, DOI 10.1017/jfm.2020.1093

- Chuvakhov PV, Borovoy VY, Egorov IV, Radchenko VN, Olivier H, Roghelia A (2017) Effect of Small Bluntness on Formation of Görtler Vortices in a Supersonic Compression Corner Flow. *Journal of Applied Mechanics and Technical Physics* 58(6):975–989, DOI 10.1134/S0021894417060037
- Chynoweth BC, Schneider SP, Hader C, Fasel H, Batista A, Kuehl J, Juliano TJ, Wheaton BM (2019) History and progress of boundary-layer transition on a Mach-6 flared cone. *Journal of Spacecraft and Rockets* 56(2):333–346, DOI 10.2514/1.A34285
- Comte P (1999) Large-Eddy Simulations of Compressible Shear Flows. In: Knight D, Sakell L (eds) *Recent Advances in DNS and LES*, Springer Netherlands, Dordrecht, pp 1–12
- Dwivedi A, Sidharth GS, Nichols JW, Candler GV, Jovanović MR (2019) Reattachment streaks in hypersonic compression ramp flow: An input-output analysis. *Journal of Fluid Mechanics* 880:113–135, DOI 10.1017/jfm.2019.702, [1811.09046](https://doi.org/10.1017/jfm.2019.702)
- Esquieu S, Benitez E, Schneider SP, Brazier JP (2019) Flow and stability analysis of a hypersonic boundary-layer over an axisymmetric cone-cylinder-flare configuration. In: *AIAA Scitech 2019 Forum*, p 2115, DOI 10.2514/6.2019-2115
- Estorf M, Radespiel R, Schneider SP, Johnson HB, Hein S (2008) Surface-pressure measurements of second-mode instability in quiet hypersonic flow. In: *46th AIAA Aerospace Sciences Meeting and Exhibit*, p 1153, DOI 10.2514/6.2008-1153
- Foysi H, Sarkar S (2010) The compressible mixing layer: An les study. *Theoretical and Computational Fluid Dynamics* 24(6):565–588, DOI 10.1007/s00162-009-0176-8
- Franko KJ, Lele S (2014) Effect of adverse pressure gradient on high speed boundary layer transition. *Physics of Fluids* 26(2):24106, DOI 10.1063/1.4864337
- Franko KJ, Lele SK (2013) Breakdown mechanisms and heat transfer overshoot in hypersonic zero pressure gradient boundary layers. *Journal of Fluid Mechanics* 730:491–532, DOI 10.1017/jfm.2013.350
- Ginoux JJ (1969) On Some Properties of Reattaching Laminar and Transitional High Speed Flows. *Heat and Mass Transfer in Flows with Separated Regions*
- Gonzales J, Suzuki K, Sakaue H (2020) Temporally and Spatially Resolved Pressure and Temperature Maps in Hypersonic Flow. *International Journal of Heat and Mass Transfer* 156:119782, DOI 10.1016/j.ijheatmasstransfer.2020.119782
- Görtler H (1940) Instabilität laminarer Grenzschichten an konkaven Wänden gegenüber gewissen dreidimensionalen Störungen. *ZAMM - Journal of Applied Mathematics and Mechanics Zeitschrift für Angewandte Mathematik und Mechanik* 21(4):250–252
- Grossir G (2017) Xperimental Characterization of Hypersonic Transitional Boundary Layers. In: *introduction to stability and transition analysis method SSEMID*, Von Karman Institute for Fluid Dynamics, DOI 10.35294/l201801.grossir
- Gudmundsson K, Colonius T (2011) Instability wave models for the near-field fluctuations of turbulent jets. *Journal of Fluid Mechanics* 689:97–128, DOI 10.1017/jfm.2011.401
- Heffner KS, Chpoun A, Lengrand JC (1993) Experimental study of transitional axisymmetric shock-boundary layer interactions at mach 5. In: *AIAA 23rd Fluid Dynamics, Plasmadynamics, and Lasers Conference*, 1993, p 3131, DOI 10.2514/6.1993-3131
- Hildebrand N, Dwivedi A, Nichols JW, Jovanović MR, Candler GV (2018) Simulation and stability analysis of oblique shock-wave/boundary-layer interactions at Mach 5.92. *Physical Review Fluids* 3(1):13906, DOI 10.1103/PhysRevFluids.3.013906, [1712.08239](https://doi.org/10.1103/PhysRevFluids.3.013906)
- Kudryavtsev AN, Khotyanovsky DV (2005) Numerical Investigation of High Speed Free Shear Flow Instability and Mach Wave Radiation. *International Journal of Aeroacoustics* 4(3):325–343, DOI 10.1260/1475472054771394
- Le Sant Y (2005) An image registration method for infrared measurements. *Quantitative InfraRed Thermography Journal* 2(2):207–222, DOI 10.3166/qirt.2.207-222
- Le Sant Y, Marchand M, Millan P, Fontaine J (2002) An overview of infrared thermography techniques used in large wind tunnels. *Aerospace Science and Technology* 6(5):355–366, DOI 10.1016/S1270-9638(02)01172-0
- Lugrin M, Beneddine S, Garnier E, Bur R (2021a) Multi-scale study of the transitional shock-wave boundary layer interaction in hypersonic flow. *Theoretical and Computational Fluid Dynamics* URL <https://doi.org/10.1007/s00162-021-00595-7>
- Lugrin M, Beneddine S, Leclercq C, Garnier E, Bur R (2021b) Transition scenario in hypersonic axisymmetrical compression ramp flow. *Journal of Fluid Mechanics* 907:A6, DOI 10.1017/jfm.2020.833, [2009.08359](https://doi.org/10.1017/jfm.2020.833)
- Lumley J (1970) *Stochastic tools in turbulence*. New York Academic
- Mack LM (1975) Linear stability theory and the problem of supersonic boundary-layer transition. *AIAA Journal* 13(3):278–289, DOI 10.2514/3.49693
- Marxen O, Rist U (2010) Mean flow deformation in a laminar separation bubble: Separation and stability characteristics. *Journal of Fluid Mechanics* 660:37–



- 54, DOI 10.1017/S0022112010001047
- Masutti D, Spinosa E, Chazot O, Carbonaro M (2011) Disturbance level characterization of a hypersonic blow-down facility. 41st AIAA Fluid Dynamics Conference and Exhibit 50(12):2720–2730, DOI 10.2514/6.2011-3887
- Murray N, Hillier R, Williams S (2013) Experimental investigation of axisymmetric hypersonic shock-wave/turbulent-boundary-layer interactions. *Journal of Fluid Mechanics* 714:152–189, DOI 10.1017/jfm.2012.464
- Navarro-Martinez S, Tutty OR (2005) Numerical simulation of Görtler vortices in hypersonic compression ramps. *Computers and Fluids* 34(2):225–247, DOI 10.1016/j.compfluid.2004.05.002
- Özgen S, KırcaI SA (2008) Linear stability analysis in compressible, flat-plate boundary-layers. *Theoretical and Computational Fluid Dynamics* 22(1):1–20, DOI 10.1007/s00162-007-0071-0
- Reynolds WC (1991) Three-dimensional simulations of large eddies in the compressible mixing layer. *Journal of Fluid Mechanics* 224:133–158, DOI 10.1017/S0022112091001684
- Roghelia A, Chuvakhov PV, Olivier H, Egorov IV (2017) Experimental investigation of Görtler vortices in hypersonic ramp flows behind sharp and blunt leading edges. In: 47th AIAA Fluid Dynamics Conference, 2017, p 3463, DOI 10.2514/6.2017-3463
- Running CL, Juliano TJ (2021) Global measurements of hypersonic shock-wave/boundary-layer interactions with pressure-sensitive paint. *Experiments in Fluids* 62(5):1–18, DOI 10.1007/s00348-021-03194-8
- Running CL, Juliano TJ, Borg MP, Kimmel RL (2020) Characterization of post-shock thermal striations on a cone/flare. *AIAA Journal* 58(5):2352–2358, DOI 10.2514/1.J059095
- Sandham ND, Reynolds WC (1990) Compressible mixing layer: Linear theory and direct simulation. *AIAA Journal* 28(4):618–624, DOI 10.2514/3.10437
- Sidharth G, Dwivedi A, Candler GV, Nichols JW (2018) Onset of three-dimensionality in supersonic flow over a slender double wedge. *Physical Review Fluids* 3(9):93901, DOI 10.1103/PhysRevFluids.3.093901
- Simeonides G (1992) Hypersonic shock wave boundary layer interactions over compression corners. PhD thesis, University of Bristol. Faculty of Engineering, Department of Aerospace
- Simeonides G, Haase W (1995) Experimental and Computational Investigations of Hypersonic Flow About Compression Ramps. *Journal of Fluid Mechanics* 283:17–42, DOI 10.1017/S0022112095002229
- Sipp D, Marquet O (2013) Characterization of noise amplifiers with global singular modes: The case of the leading-edge flat-plate boundary layer. *Theoretical and Computational Fluid Dynamics* 27(5):617–635, DOI 10.1007/s00162-012-0265-y
- Sirovich L (1987) Turbulence and the dynamics of coherent structures. III. Dynamics and scaling. *Quarterly of Applied Mathematics* 45(3):583–590, DOI 10.1090/qam/910464
- Threadgill JA, Little JC, Wernz SH (2021) Transitional shock boundary layer interactions on a compression ramp at mach 4. *AIAA Journal* pp 1–18
- Towne A, Schmidt OT, Colonius T (2018) Spectral proper orthogonal decomposition and its relationship to dynamic mode decomposition and resolvent analysis. *Journal of Fluid Mechanics* 847:821–867, DOI 10.1017/jfm.2018.283, [1708.04393](https://doi.org/10.1017/jfm.2018.283)
- Vandomme L (2004) Contribution à l'étude de l'interaction onde de choc couche limite transitionnelle en écoulement hypersonique à Mach 5. thèse de doctorat, ONERA
- Vermeulen J, Simeonides G (1992) Parametric studies of shock wave/boundary layer interactions over 2 d compression corners at mach 6. Tech. rep., VKI
- Yang L, Zare-Behtash H, Erdem E, Kontis K (2012) Investigation of the double ramp in hypersonic flow using luminescent measurement systems. *Experimental Thermal and Fluid Science* 40:50–56, DOI 10.1016/j.expthermflusci.2012.01.032

## Appendix 1 : PCB sensors integration

This appendix describes the integration technique used to be able to flush-mount PCB sensors on the model and to protect them from thermal effects. As presented in figure 22, the integration of a flat sensor on a curved surface leads to the apparition of discontinuities at the sensor/model junction. While this step may be tolerable for models such as the one used here, it may become extremely problematic for models like cones, where the radius of curvature can be small. To solve this problem (and to protect the sensor from thermal effects), an epoxy layer has been added on top of the sensor such as presented in figure 23, this layer can be surfaced once mounted on the model to be as flush as possible (see figure 24). The steps between the sensors surface and the model surfaces have been measured using the Mahr MarSurf M 400 to be less than 40µm.

However, this added layer of epoxy might change significantly the response of the sensor. To quantify the change in transfer function caused by the modification, shock-tube calibrations of the same sensor with and



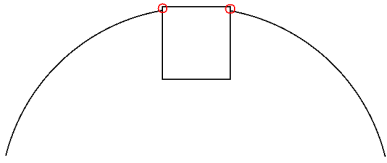


**Fig. 22** Schematic of the integration problem



**Fig. 23** PCB sensor with an added epoxy layer

without the added epoxy layer have been conducted. Results are presented in figure 25, which shows that the epoxy layer is only slightly shifting the resonance frequency toward lower frequencies. The amplitude of the resonance is also increased. Apart from that, no clear difference can be found between the transfer functions with and without epoxy. The resonance of the sensor visible in those results has also been documented in several other studies (Grossir, 2017; Butler and Laurence, 2021a).

While the shock-tube calibration brings confidence toward the good behavior of the PCB with epoxy, a last effort was made to ensure the quality of the results. A comparison of the spectrum produced by a PCB sensor in the turbulent region of the flare was compared to the one produced by a numerical simulation reproducing the experiment. While the numerical-experimental comparison is out of the scope of this study, figure 26 confirms that the behavior of the PCB with epoxy is excellent in the turbulent region.



**Fig. 24** PCB sensor mounted on the model

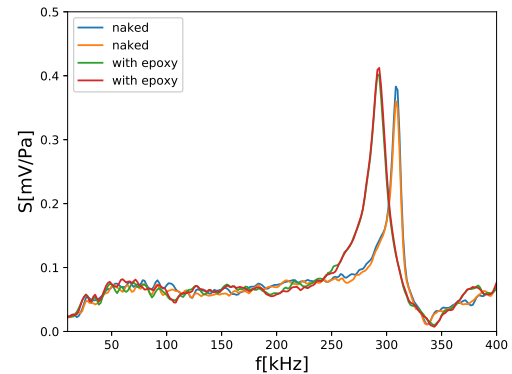


**Fig. 25** Shock-tube calibration of the same sensor with and without the added epoxy layer, two runs are presented for each case to show the good reproductibility of the results.

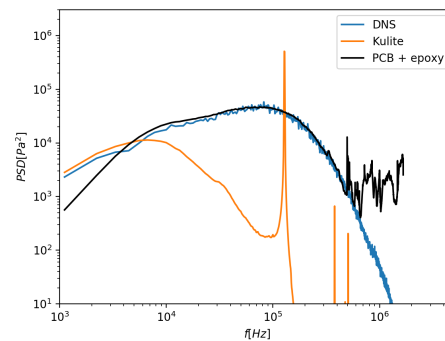


**Fig. 26** Turbulent flow validation against computational results, the computation used here is overall very similar to the one presented in Lugin et al. (2021b).